RSC Advances

ROYAL SOCIETY OF CHEMISTRY

www.rsc.org/advances

Phase and morphology evolution of VO_2 nanoparticles using a novel hydrothermal system for thermochromic applications: the growth mechanism and effect of ammonium (NH_4^+)

Bingrong Dong, [1] *Nan Shen,* [1] *Chuanxiang Cao,* [1] *Zhang Chen,* [2] *Hongjie Luo,*[1,2] *Yanfeng Gao*[1,2,3*]

1 State Key Laboratory of High Performance Ceramics and Superfine Microstructure, Shanghai institute of Ceramics, Chinese Academy of Sciences, 1295 Dingxi, Shanghai 200050, China

2 School of Materials Science and Engineering, Shanghai University, 99 Shangda, Shanghai 200444, China

3 Key Laboratory for Palygorskite Science and Applied Technology of Jiangsu Province, Jiangsu Provincial Engineering Laboratory for Advanced Materials of Salt Chemical Industry, Huaiyin Institute of Technology, Huaian 223003, People's Republic of China

* Author for correspondence. Email: yfgao@shu.edu.cn

Tel/Fax: +86-21-6990-6218

Abstract

To reveal the formation mechanism of VO_2 nanomaterials in a hydrothermal system, an experimental method was designed to study the growth and crystallization of VO_2 nanomaterial by combining the reduction of V_2O_5 and the homogeneous precipitation methods. For Route A without the addition of ammonium, VO_2 (B) nanobelts were assembled by $(VO_2)_x \cdot yH_2O$ thin nano-slices, and for Route B in the presence of ammonium, the VO_2 (M) nanoparticles were decomposed from $(NH_4)_2V_4O_9$ sheets. The ammonium solution played a crucial role in the formation of the $(NH_4)_2V_4O_9$ intermediate phase and finally to VO_2 (M) nanoparticles. Therefore, by contrasting Routes A and B, our results revealed that the ammonium (NH_4^+) ion changed the reaction process and significantly influenced the preparation of well-crystallized VO_2 (M) nanoparticles under hydrothermal conditions. The obtained VO_2 (M) nanoparticles exhibited a high phase transition enthalpy (ΔH = 32.4 J/g). The VO_2-PET composite films that were derived from these VO_2 (M) nanoparticles exhibited excellent optical switching characteristics (T_{lum} = 33.5%, ΔT_{sol} = 16.0%). Moreover, W-doped VO_2 nanoparticles with different W doping levels were also prepared. The efficiency of W^{6+} dopants to lower the transition phase temperature (Tc) was determined to occur at a rate of 19.8 K/at.%.

Keywords: Vanadium dioxide; growth mechanism; thermochromic;

1 Introduction

In recent years, monoclinic/rutile vanadium dioxide VO_2 (M/R) has attracted extensive attention as a promising candidate for smart window applications due to its unique reversible metal–insulator transition (MIT) at a critical temperature of 68 ℃ (341 K)[1]. The MIT occurs when the high-temperature tetragonal rutile structure of VO_2 (R, $P4_2/mnm$) transforms into a low-temperature monoclinic structure (M, $P2_1/c$), accompanying by dramatic changes in its near-infrared optical properties[2]. Therefore, VO_2 thermochromic smart windows can regulate solar energy transmission and maintain high luminous transmittances by responding to the ambient temperature without the use of any external switching device[3-5].

As one of the most conventional synthesis methods, the hydrothermal method has been employed to prepare nanoscale VO_2 (M) with various morphologies. However, due to complicated factors, such as the number of metastable polymorphic structures of VO_2 (VO_2 (B)[6], VO_2 (A)[7] and VO_2 (D)[8]) and the multivalence of vanadium (from V^{3+} to V^{5+}), the reaction condition must to be accurately controlled. According to previous studies, vanadium oxides with the desired phase compositions can be synthesized using several systems including the reduction of pentavalent vanadium compounds (V_2O_5 or NH_4VO_3) with reducing agents (oxalic acid[9, 10], diamide hydrochloride[11, 12] or EG[13, 14]) as well as homogeneous precipitation of $VOSO_4$ under mild hydrothermal conditions[15, 16].

All these systems have a similar mechanism (i.e., the precursors of the V^{4+} compounds were transformed to VO_2 (M) in a typical hydrothermal process). For the V_2O_5 and oxalic acid system, the metastable phase VO_2 (B) nano-belts were often obtained at a lower synthesis temperature during the hydrothermal reaction.[17] VO_2 (B) can be further transformed to VO_2 (M) by increasing the hydrothermal temperature and time, and the final VO_2 (M) products exhibited mostly one-dimensional morphologies, such as nanobelts, nanowires, nanorods or snowflakes assembled using VO_2 (M) rods.[18] However, for the V_2O_5 and diamide hydrochloride system, a new intermediate phase $(NH_4)_2V_4O_9$ was observed during the hydrothermal process.[19] To

further evaluate the effect of the intermediate $(NH_4)_2V_4O_9$, a "two-step" hydrothermal process was designed to study the evolution from $(NH_4)_2V_4O_9$ to VO_2 (M). The intermediate phase $(NH_4)_2V_4O_9$ was first prepared at 230 °C and then decomposed to VO_2 (M) nanoparticles by rapidly heating up to 280 – 300 °C.[19] Due to the complexity of VO_2 growth, the various morphologies of VO_2 (M) as well as the different growth mechanisms under hydrothermal condition must be investigated.

In the current study, a novel system was designed that combines the V_2O_5 and oxalic acid system and the homogeneous precipitation of $VOSO_4$. Two routes without and with the addition of an $NH_3 \cdot H_2O$ solution were used to study the effect of ammonium (NH_4^+) on the growth and crystallization of VO_2. In Route A without the addition of ammonium, VO_2 (B) nanobelts were assembled by an unknown vanadium oxide hydrate. However, in Route B in the presence of ammonium, VO_2 (M) nanoparticles were decomposed by the $(NH_4)_2V_4O_9$ sheets, which were piled by the vanadium oxide hydrate $(VO_2)_x \cdot yH_2O$. The ammonium ion (NH_4^+) played a crucial role in the formation of the $(NH_4)_2V_4O_9$ intermediate phase, which led to the synthesis of VO_2 (M) nanoparticles. The crystalline VO_2 (M) nanoparticles prepared by Route B exhibited a high latent heat during MIT (ΔH = 32.4 J/g). In addition, a film derived from these VO_2 (M) nanoparticles exhibited excellent thermochromic optical properties (T_{lum} = 33.5%, ΔT_{sol} = 16.0%). Moreover, the VO_2 (M) nanoparticles with different W-doping contents were also investigated and the efficiency of the W^{6+} dopant to lower the transition phase temperature (Tc) was determined to occur at a rate of 19.8 K/at.%.

2 Experimental Methods

2.1 Sample preparation

All the reagents in this study were purchased from the Sinopharm Chemical Reagent Co., Ltd., and used without further purification. In a typical hydrothermal synthesis, 0.25 g vanadium pentoxide (V_2O_5, analytically pure) were added to 80 mL of 0.30 M aqueous $H_2C_2O_4 \cdot 2H_2O$ to form a yellowish slurry. The slurry was continuously stirred

until a clear dark blue solution (VO^{2+}) formed. Then, the appropriate amount of a sodium hydroxide solution was added to the solution under continuous stirring. The pH of the resulting solution was adjusted to 7 using a sodium hydroxide solution (NaOH, 1.0 mol/L). A brown precursor formed when the NaOH solution was added, and the precursor was collected by centrifugation, as shown in Fig. 1.

Route A: The brown precursor was dispersed in 30 mL of deionized water. The total volume of the precursor solution was transferred to a 50 mL stainless steel autoclave followed by hydrothermal treatment under auto-generated pressure at 280 ℃ for different periods of time ranging from 1 to 24 h. The final black product was separated using centrifugation, washed with deionized water and ethanol and dried in a vacuum drying oven at 60 ℃ for 24 h.

Route B: The brown precursor was dispersed in 30 mL of deionized water, and 0.2 ml of an $NH_3 \cdot H_2O$ (28 wt %) solution was added to the precursor solution. The total volume of the precursor solution was transferred to a 50 mL stainless steel autoclave. The subsequent operations were the same as those for Route A. To reduce the phase transition temperature of VO_2, different amounts of ammonium tungstate $(NH_4)_{10}W_{12}O_{41} \cdot 5H_2O$ were added prior to sealing the stainless steel autoclave.

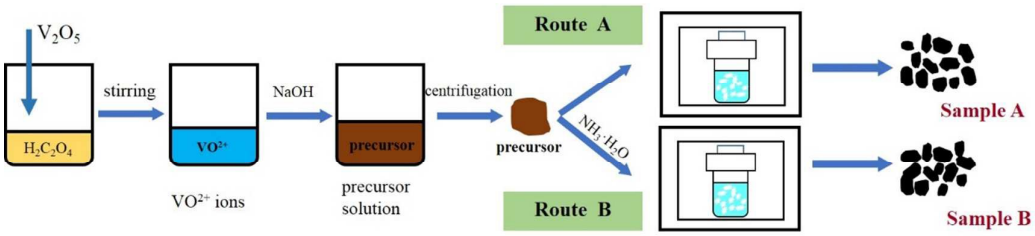

Fig. 1 Schematic flowchart for the synthesis via a novel hydrothermal system.

2.2 Characterization

The morphologies of the resulting powders were analysed via transmission electron microscopy (TEM, JEM2010, JEOL, Japan) and scanning electron microscopy (SEM, Magellan 400), respectively. The crystalline phases of the nanoparticles were determined by X-ray diffraction (XRD, Model D/Max 2550 V, Rigaku, Japan). The

decomposition process of the intermediate phase was investigated by thermogravimetry (TG, STA 449C, Netzsch, Selb, Germany) at a heating rate of 10 °C/min^{-1}.The phase transition temperatures of the products were measured via differential scanning calorimetry (DSC, DSC200F3, NETZSCH) in nitrogen flow at a heating rate of 10 °C min^{-1}. Fourier transform infrared spectroscopy (FTIR, Nicolet, Magna 560) was used to detect the chemical bonding of the samples. The Raman spectra of the composite samples were recorded using a Raman microscope (Renishaw in Via) with a 514 nm laser source at an input power of 1 mW. The thermochromic properties were evaluated by the VO_2-PET composite films. For measurements, the VO_2 powders were uniformly dispersed in polyurethane after surface modification by poly(vinylpyrrolidone) (PVP) followed by deposition on polyethylene terephthalate (PET) via knife-coating, and finally dried at 70 °C. The optical transmittance characteristics were monitored using a Hitachi U-4100 UV-visible-near-IR spectrophotometer equipped with a film heating unit in the wavelength range of 350-2600 nm. For all the samples, the integral visible transmittance (T_{lum}, 350 - 750 nm) and solar transmittance (T_{sol}, 240 - 2600 nm) were obtained based on the measured spectra using the following equation:

$$T_i = \int \varphi_i(\lambda) T(\lambda) d\lambda / \int \varphi_i(\lambda) d\lambda \qquad (1)$$

$$\Delta T_{sol} = T_{sol}(T < T_c) - T_{sol}(T > T_c) \qquad (2)$$

where $T(\lambda)$ denotes the transmittance at wavelength λ, i denotes 'lum' or 'sol' for the calculations, T and ΔT_{sol} are the temperature and solar modulation ability, respectively; φ_{lum} is the standard luminous efficiency function for the photopic vision according to CIE 1931 standards, and φ_{sol} is the solar irradiance spectrum for the air mass 1.5 (corresponding to the sun standing 37° above the horizon) according to ASTM G173-03 Reference Spectra.

3 Results and discussion

3.1 Analysis of the synthesis via Routes A and B

Among all the developed synthetic methods, the hydrothermal method based on a

water system utilizes chemical reactions and solubility changes of the substances to prepare inorganic nanostructures.[20] An appropriate precursor or a precursor solution is key to successful preparation of the target products. In this study, a brown precursor was obtained from the precipitation of the reduced VO^{2+} ions and NaOH. According to previous studies[12, 19, 21], the amorphous precursor was a six-coordinated zero-charge monomer $[VO(OH)_2(OH_2)_3]$. From the XRD pattern (Fig. 2a), the precursor without any peak was amorphous form. The FTIR spectrum of the obtained precursor was shown in Fig. 2b. The sharp absorption peaks at 555, 989 and 1092 cm^{-1} were attributed to the stretching vibrations of V-O and V=O, while the peaks at 800 cm^{-1} corresponds to the bending vibrations of V-O-V. The other two peaks at about 1629 and 3250 cm^{-1} were attributed to O-H stretching and H-O-H bending vibration modes of H_2O molecules, respectively. In Fig. 2c, based on the TG-DSC curve, the decomposition reaction of the precursor contained two stages, which occurred at 103 °C and approximately 230 °C. The TG curve showed a weight loss of about 18% from 65 to 220 °C due to the evaporation of H_2O and with the temperature increasing, the weight gained about 1% due to the oxidation of vanadium oxide (IV). Therefore, the broad peak at 230 °C was attributed the transformation from $(VO_2)_x$ to VO_2. The lowest hydrothermal temperature for the formation of VO_2 was approximately 230 °C.

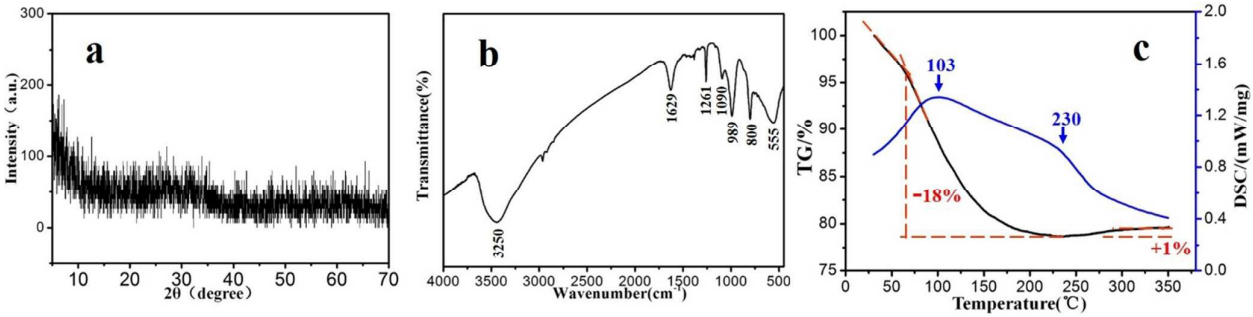

Fig. 2 The XRD pattern, FTIR spectrum and TG-DSC curve for the brown precursor.

However, through Routes A and B, different phases including VO_2 (B) and VO_2 (M) were prepared using the same precursor. Fig. 3a shows the XRD patterns of the synthetic products obtained from Route A and the phase evolution as a function of reaction time. An unknown phase with peaks at 7°, 16°, 19.8°, 27° and 30.5° was generated and did not match any vanadium oxide or hydrated vanadium oxide phase

in the ICDD PDF database. This phase is mostly likely a type of vanadium oxide hydrate $(VO_2)_x \cdot yH_2O$[19]. When reaction time was increased to 2 h, the 7° peak weakened, and a mixture of $(VO_2)_x \cdot yH_2O$ and VO_2 (B) (JCPDS No.: 81-2392) was detected. With a further increasing in time, VO_2 (B) was ultimately prepared without other impure phases, and the enhancement of the peak at 25.2° for VO_2 (B) indicated improved crystallinity. However, for Route B in Fig. 3b, the XRD patterns suggested that the final product was VO_2 (M). A mixture of $(VO_2)_x \cdot yH_2O$ and $(NH_4)_2V_4O_9$ (JCPDS No. 23-0791) was formed after 1 h, which was mostly likely caused by the introduction of the NH_4^+ ions. On the influence of the NH_4^+ ions, the vanadium oxide hydrate $(VO_2)_x \cdot yH_2O$ gradually transformed to $(NH_4)_2V_4O_9$, which differed from the phase evolution in Route A. Simultaneously, the characteristic peaks of VO_2 (M) (JCPDS No.: 72-0514) were observed after 2 h. The XRD intensity of the VO_2 (M) peaks were significantly enhanced from 6 h to 24 h, indicating substantial improvement of the crystallinity. In summary, two different hydrothermal processes (Routes A and B) using the same precursor resulted in different products, indicating that a certain amount of $NH_3 \cdot H_2O$ influenced the synthesis of the VO_2 polymorphs. The purpose of the introduction of NH_4^+ ions was on changing the reaction process and promoting the formation of $(NH_4)_2V_4O_9$ instead of directly reacting to VO_2 (B) in Route A. The evolutions of Routes A and B occurred as follows:

Route A: $VO^{2+} \rightarrow (VO_2)_x \cdot yH_2O \rightarrow VO_2$ (B)

Route B: $VO^{2+} \rightarrow (VO_2)_x \cdot yH_2O + NH_3 \cdot H_2O \rightarrow (NH_4)_2V_4O_9 \rightarrow VO_2$ (M)

The effect of the quantity of ammonium ion on the synthesis of VO_2 was also studied. From the XRD patterns (Fig. 3c) with the addition of different quantities of $NH_3 \cdot H_2O$ solution, all the reaction products were indexed to VO_2 (M) without other impure phases. But the (011) peaks of VO_2 (M) gradually decreased and broadened with the quantity of $NH_3 \cdot H_2O$ solution from 0.1 ml to 0.6 ml. It revealed that with the increase of the quantity of $NH_3 \cdot H_2O$, the crystallinity gradually weakened or the grain size of VO_2 (M) nanoparticles decreased.

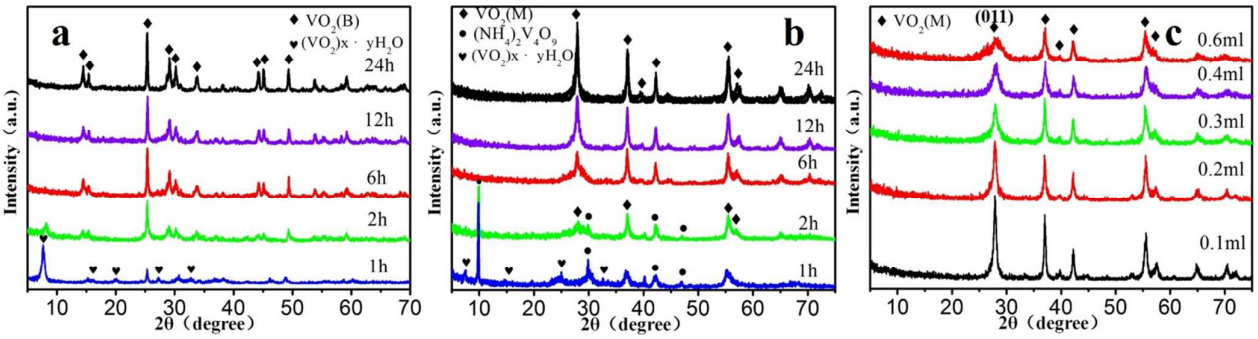

Fig. 3 XRD patterns of the obtained samples via (a) Route A without the additional $NH_3 \cdot H_2O$ solution and (b) Route B with the additional $NH_3 \cdot H_2O$ solution at 280 °C for different periods of time; (c) The XRD patterns of the reaction products after adding different quantities of $NH_3 \cdot H_2O$ solution.

3.2 Analysis of the morphological and transformational mechanisms

To further confirm the XRD results and monitor the morphological evolution, the SEM images of the products prepared via Routes A and B were shown in Fig. 4. For Route A, thin $(VO_2)_x \cdot yH_2O$ nano-slices with a length of 200-600 nm and a width of 50-150 nm (Fig. 4a) were first observed at 280 °C after 1 h. As the reaction time increased, the short and thin nano-slices piled up and further grew into larger VO_2 (B) nano-belts. Fig. 4b showed the coexistence of $(VO_2)_x \cdot yH_2O$ and VO_2 (B) with inhomogeneous nano-belts. After $(VO_2)_x \cdot yH_2O$ was completely transformed to VO_2 (B), abundant uniform nano-belts that were 500-1000 nm in length and 100-400 nm in width were observed (Fig. 4c). The VO_2 (B) nano-belts continued to grow longer and thicker and finally became long strips after 24 h (Fig. 4d). However, for Route B, a mixture of thin $(VO_2)_x \cdot yH_2O$ slices and large $(NH_4)_2V_4O_9$ sheets were first observed after 1 h, as shown in Fig. 4e. Then, the small slices disappeared, and the VO_2 (M) nanoparticles were generated without the emergence of VO_2 (B) nano-belts, as shown in Fig. 4f. With a further increase in the reaction time, $(NH_4)_2V_4O_9$ sheets were ultimately transformed into VO_2 (M) nanoparticles. However, the VO_2 (M) nanoparticles shown in Fig. 4g were agglomerated and surrounded by amorphous substances with poor crystallinity. When the reaction time was prolonged to 24 h, the uniform and well-crystallized VO_2 (M) nanoparticles with a sharp outline were shown

in Fig. 4g and the grain size increased slightly.

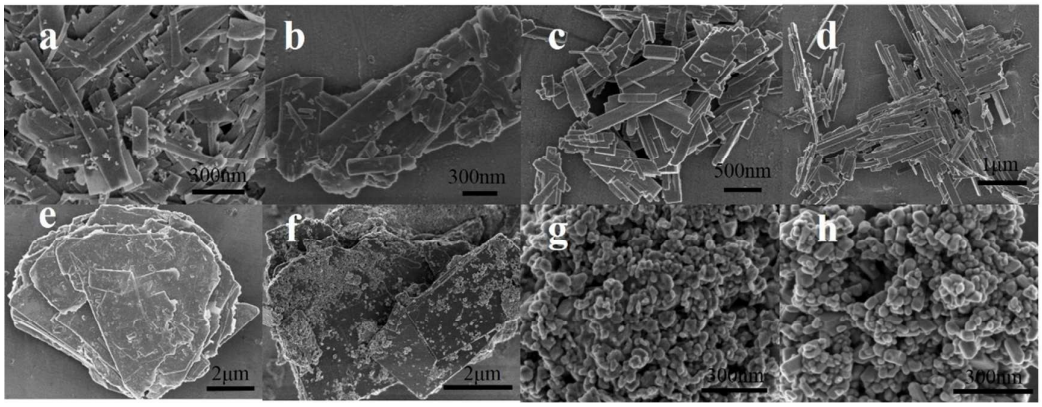

Fig. 4 SEM images of the samples obtained via Route A at 280 °C for (a) 1 h, (b) 2h, (c) 6h, (d) 24 h, via Route B for (e) 1 h, (f) 2h, (g) 6h, (h) 24 h.

In the meaning time, the SEM images of the reaction products after adding different quantities of $NH_3 \cdot H_2O$ solution were shown in Fig. 5. The differences of the morphologies of VO_2 (M) between Fig. 5a and Fig. 5f were obvious. When the addition of $NH_3 \cdot H_2O$ solution was 0.1 ml, the morphology of VO_2 (M) consist of nano-rods (~150 nm) and nanoparticles (~50nm) in Fig. 5a. With the quantity of $NH_3 \cdot H_2O$ solution increasing, the nano-rods shortened and the nanoparticles diminished. Thus when the addition of $NH_3 \cdot H_2O$ solution reached 0.4 ml, the grain size showed uniform and were around 40 nm in Fig. 5e.

Therefore, the quantity of $NH_3 \cdot H_2O$ influence the synthesis of VO_2 (M) nanoparticles. For reaction (1), the increase of $NH_3 \cdot H_2O$ could facilitate the formation of $(NH_4)_2V_4O_9$; but for reaction (2), the increase of $NH_3 \cdot H_2O$ significantly restrained the decomposition of $(NH_4)_2V_4O_9$ so that the less VO_2 nucleus were produced. Finally, the nucleation-recrystallization-growth process to form VO_2 (M) nanoparticles was restrained. Thus, with the quantity of $NH_3 \cdot H_2O$ solution increased, the nano-rods shortened and ultimately disappeared and the grain size of VO_2 nanoparticles gradually decreased with the $NH_3 \cdot H_2O$ solution from 0.1 ml to 0.6 ml.

$$4(VO_2)_x \cdot yH_2O + 2xNH_3 \cdot H_2O \rightarrow x(NH_4)_2V_4O_9 + (x+y)H_2O \quad (1)$$

$$(NH_4)_2V_4O_9 \rightarrow 2NH_3 + H_2O + 4VO_2\ (M) \quad (2)$$

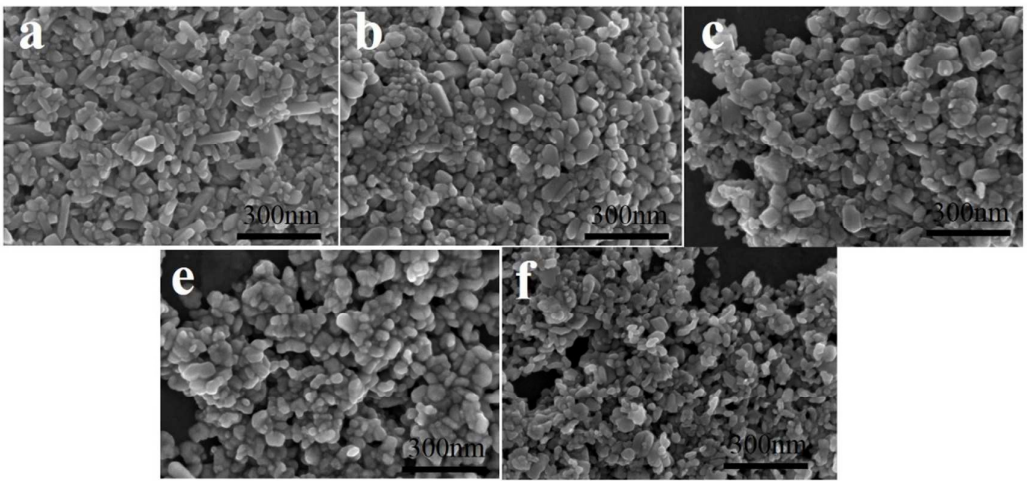

Fig. 5 The SEM images of the reaction products after adding different quantities of NH3·H2O solution.

Fig. 6 showed the TEM images of samples prepared via Route A. The thin $(VO_2)_x \cdot yH_2O$ nano-slices that were 500 nm in length (Fig. 6a) and VO_2 (B) nano-belts with a typical rectangular structure (Fig. 6b) were prepared after 1 h and 6 h, respectively. After 24 h, the nano-belts grew into long strips with several micrometers, as shown in Fig. 6c. Fig. 6d showed a representative TEM image of a VO_2 (B) nano-belt that was oriented and attached by several little belts. A high-resolution TEM (HRTEM) study revealed its high crystallinity combined with the corresponding selected area electron diffraction (SAED). The well-resolved lattice fringes (Fig. 6e selected from the yellow frame in Fig. 6d and Fig. 6f selected from the green frame in Fig. 6d) with an interplanar spacing of 0.582 nm were consistent with the (200) plane spacing of monoclinic VO_2 (B), which indicated a (001) preferential growth direction for monoclinic VO_2 (B). Moreover, the oriented-attached nano-belts shared the same crystal orientation and were interconnected via their edges or surfaces. This result further confirmed the occurrence of the self-assembled combination during Route A.

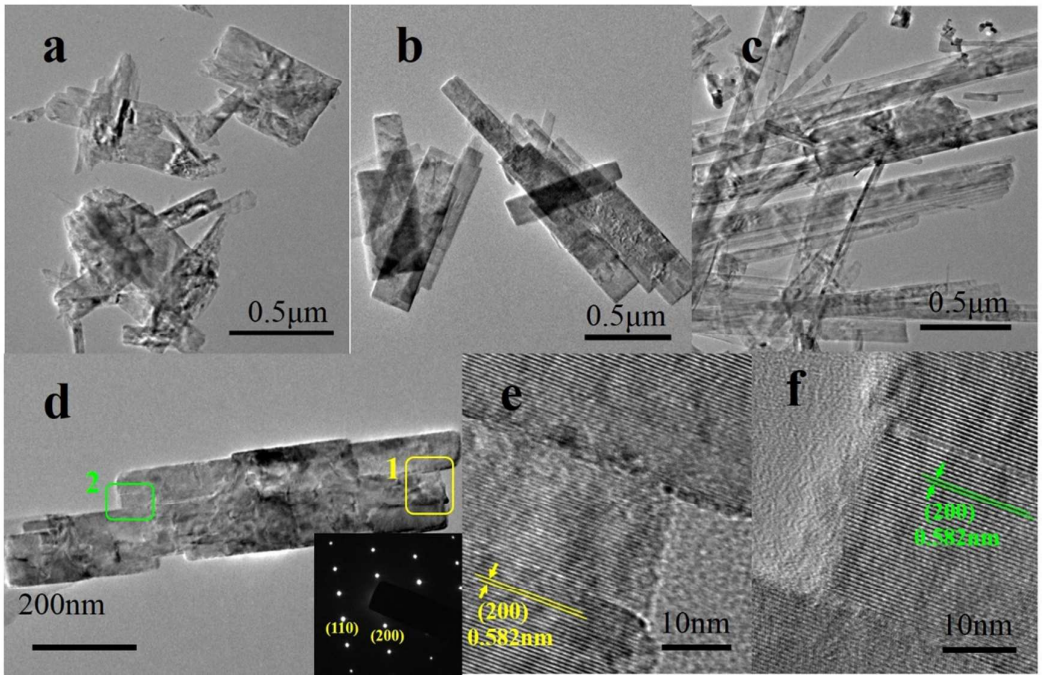

Fig .6 TEM images of the samples obtained via Route A at 280 °C for (a) 1 h, (b) 6 h, (c) 24 h and (d, e, f) 3 h.

For Route B, along with the phase evolution (i.e. $VO^{2+} \rightarrow (VO_2)_x \cdot yH_2O \rightarrow (NH_4)_2V_4O_9 \rightarrow VO_2$ (M)), the morphology gradually changed from nano-slices to square sheets and finally to nanoparticles as the reaction time increased. A mixture of nano-slices and square sheets was observed after 1 h (Fig. 7a). After 2 h, $(NH_4)_2V_4O_9$ square sheets that were 2 μm wide were obtained, upon with a small quantity of VO_2 (M) nanoparticles dispersed on the sheets. When the reaction time was 24 h, uniform VO_2 (M) nanoparticles with an average size of 50 nm were observed, as shown in Fig. 7c. The corresponding SAED image of a single VO_2 (M) nanoparticle (Fig. 7d (inset)) was indexed to a zone axis of [2-21], which indicated that the nanoparticle was in a single crystal form. The lattice-resolved HRTEM image selected from an area in the blue frame was shown in Fig. 7d (inset), and the interplanar spacing was calculated to be approximately 0.322 nm, which was indexed to the (011) facet of VO_2 (M).

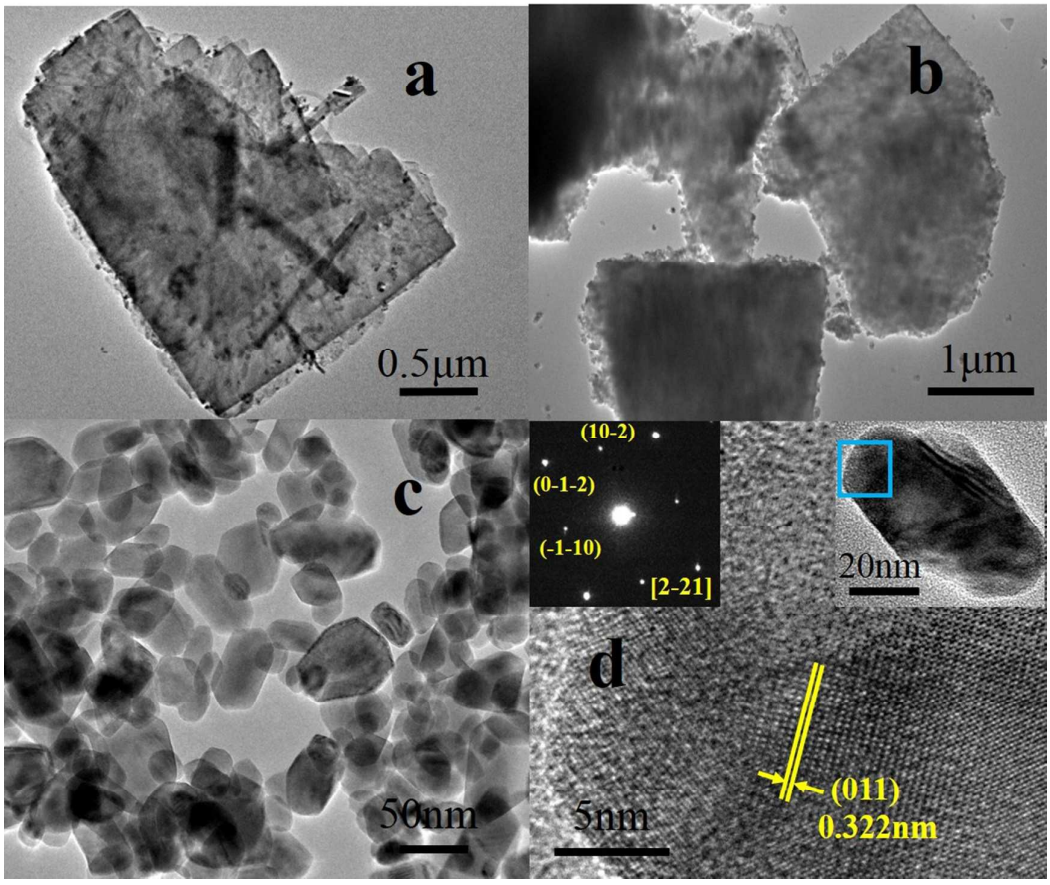

Fig .7 TEM images of the samples obtained via Route B at 280 °C for (a) 1 h, (b) 2 h, (c) 6 h and (d) 24 h.

Based on the SEM and TEM results, a proposed schematic description of the formation process of various VO_2 polymorphs via Routes A and B is illustrated in Fig. 8. After the reduction of V_2O_5, V^{4+} existed in the VO^{2+} form in acidic solutions, and the six-fold coordinated neutral monomers $[VO(OH)_2(OH_2)_3]$[19, 22] was regarded as the reactive monomer. The combination occurs either via an olation or an oxolation process as follows[23]

Olation V-OH + V-OH_2 → -V-OH-V- + H_2O (fast)

Oxolation V-OH + HO-V- → -V-O-V- + H_2O (slow)

During the olation reaction, the corner-linked octahedrons form chains along the H_2O–V–OH direction and the edge-linked octahedrons connect along HO–V–OH direction in an oxolation process[24]. In the z direction (H_2O–V=O), no H_2O–V–OH

groups exist, leading to the formation of a 1D/2D-vanadium oxide network within the xy plane[25, 26]. Under hydrothermal synthesis conditions, nano-slices of an unknown hydrate $(VO_2)x{\cdot}yH_2O$ are formed in this case. Therefore, the thin $(VO_2)x{\cdot}yH_2O$ nano-slices have a significant influence on the formation of the subsequent products from Routes A and B.

For Route A without the addition of $NH_3{\cdot}H_2O$ solution, the nano-slices are attached in a self-assembled arrangement and interconnected via edges or surfaces and ultimately reassemble into VO_2 (B) nano-belts along a preferred [001] orientation. However, for Route B, due to the effect of $NH_3{\cdot}H_2O$, the thin nano-slices form piles through stacking and finally grows into $(NH_4)_2V_4O_9$ square-sheets. The NH_4^+ ions introduced from the $NH_3{\cdot}H_2O$ solution interconnect the $(VO_2)x{\cdot}yH_2O$ layers, pushing the limit of oriented growth. Therefore, in comparison to the process of $(VO_2)x{\cdot}yH_2O$ to VO_2 (B), the NH_4^+ ions allow for a more facile transformation from $(VO_2)x{\cdot}yH_2O$ to $(NH_4)_2V_4O_9$ by substantially lowering the driving force. Based on the XRD results, the 7° peak for $(VO_2)x{\cdot}yH_2O$ disappeared more rapidly in Route B than in Route A under the same hydrothermal conditions, as shown in Fig. 2. As the reaction time increased further, the $(NH_4)_2V_4O_9$ sheets gradually decompose and finally transform into fine crystalline VO_2 (M) nanoparticles[19]. Based on the results from the two routes, the addition of the $NH_3{\cdot}H_2O$ solution is pivotal for the formation of $(NH_4)_2V_4O_9$ as well as its further decomposition into well-crystallized VO_2 (M) nanoparticles.

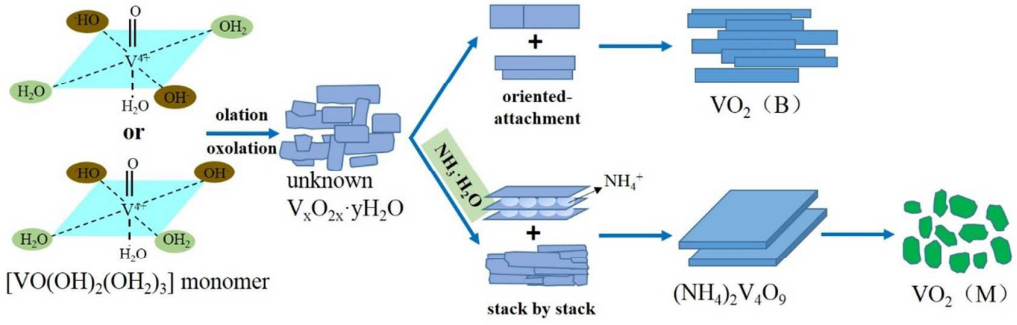

Fig. 8 Schematic illustration of the evolution of the reaction processes in Routes A and B.

The metal–insulator transition (MIT) of the VO_2 (M) nanoparticles prepared from Route B was measured by DSC and the results were shown in Fig. 9a. The VO_2 (M) nanoparticles exhibited an excellent MIT property with a phase transition enthalpy

(ΔH) of 32.4 J/g and a phase transition temperature (Tc) of 66.6 °C, which was slightly lower than that of bulk VO_2 (68 °C)[1]. Furthermore, the Raman spectra was used to record the phase transition behavior of the VO_2 nanoparticles in Fig. 9b. The characteristic peaks at 190, 222, 310, 387 and 610 cm^{-1} denoted by blue lines were ascribed to the vibration modes in VO_2 (M) from 25 to 50 °C. In addition, the M phase of VO_2 gradually transformed to the R phase during the heating process and the M-R phase transition was completed at 70 °C, which was consistent with the DSC result.

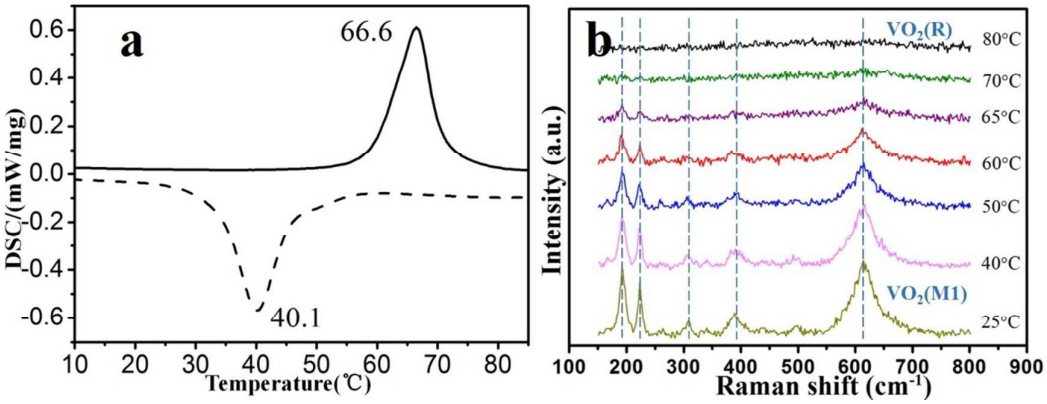

Fig. 9 (a) DSC curves and (b) characteristic Raman spectra for the VO_2 (M) nanoparticles obtained from Route B at 260 °C after 24 h.

3.3 Analysis of the W-doped VO_2 (M)

Since the Tc (66 °C) of obtained VO_2 (M) was slightly higher than room temperature, W-doping was employed to decrease the Tc to meet the requirement for thermochromic applications.[27, 28] W-doped VO_2 nanoparticles at different doping levels was characterized using ICP in Table 1. Fig. 10a provides the XRD patterns of the samples with various W doping contents, and all the peaks were indexed to VO_2 (M) without tungstic acid or other impurities. The shifting of the main peak (011) to small angles was detected in Fig. 10b, and this shift could be attributed to the substitution of W^{6+}, which had a larger radius than V^{4+}. As the W doping fraction increased from 0 to 2.05 at%, the increase in the number of W^{6+} ions in the VO_2 lattice resulted in a larger interplanar distance and a slightly increased shift to small

angles (Fig. 10b). Fig. 10c and 10d showed the W scanning TEM curves in one W doping VO_2 nanoparticle and the compositional scanning TEM curves with W, V and O atoms, respectively. These results confirmed the existence of W with a relatively uniform distribution in the VO_2 crystalline structure. Furthermore, the W atoms have been successfully incorporated into the crystal lattice of VO_2 (M).

Table 1 Plasma emission spectra analysis results of the W content in VO_2.

Expected value W (%)	0.5	1.0	1.5	2.0
ICP W (%)	0.65	1.13	1.57	2.05

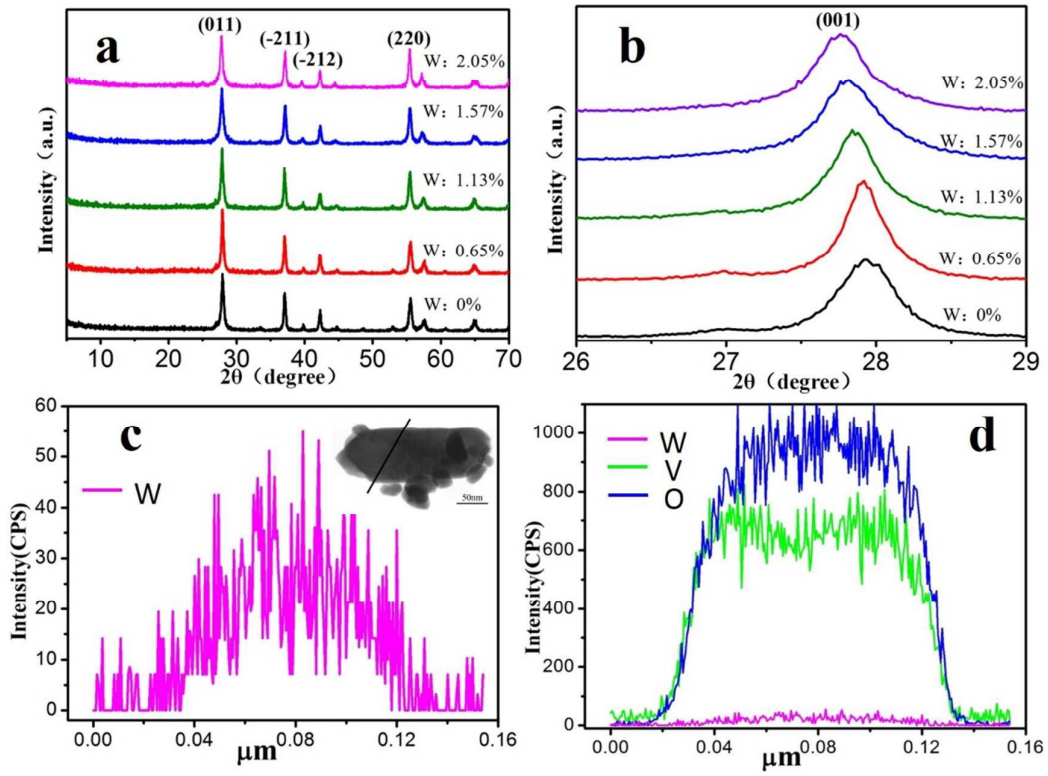

Fig. 10 (a) XRD patterns and (b) magnified patterns of the (011) peak of the as-prepared VO_2 nanoparticles with different W-doping fractions. (c) W scanning TEM curves in one VO_2 nanoparticle with a W doping fraction of 2% (inset), (d) Compositional scanning TEM curves with W, V and O atoms.

The Tc of the W-doped VO_2 nanoparticles with different doping content was investigated using DSC in Fig. 11a. The pure VO_2 exhibited a Tc value of 66.6 °C. However, for W-doped VO_2, the Tc value was reduced to 57.5, 50.4, 38.4 and 26.7 °C

from 0.65 to 2.05 at% W doping, respectively. Based on linear fitting of the Tc and W doping content shown in Fig. 11b, the Tc of VO_2 (M) decreased by 19.8 K per at% W, which is consistent with previous results[29]. This phenomenon may be related to changes in the crystalline structure and electronegativity differences. According to the research reported by Tang et al.[30], the charger transfer resulting from W doping weakened the V^{4+}-V^{4+} pairs, destabilizing the semiconducting phase of VO_2 and promoting the phase transition from monoclinic to rutile. In addition, Booth et al.[2] proposed that the significant expansion in the crystal structure induced by W doping broke the V-V homopolar bonds, which led to a decrease in Tc. Simultaneously, the high valence of W^{6+} increased the concentration of free electrons, which promoted the transition at lower temperatures.[31] Therefore, W atoms can be effectively doped into the VO_2 lattice to tune down the Tc.

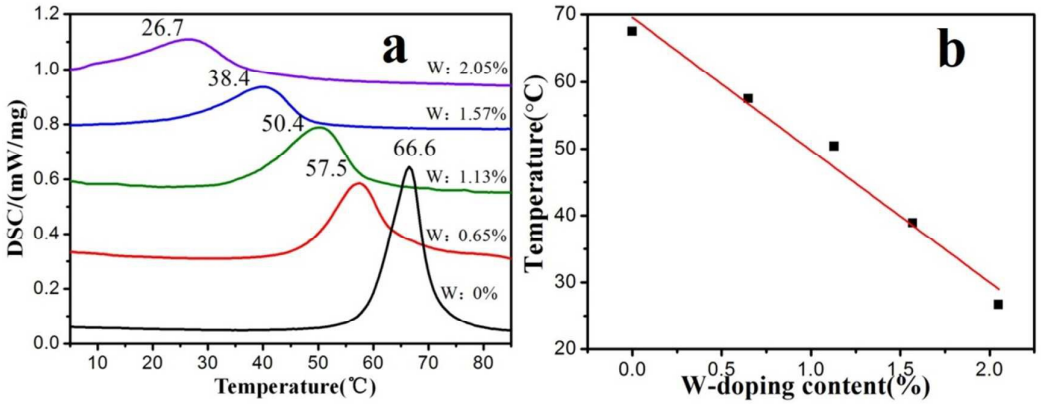

Fig. 11 (a) DSC curves of VO_2 nanoparticles with different W doping fractions. (b) Tc data with linear fitting for the as-prepared VO_2 nanoparticles with different W doping fractions.

The thermochromic optical properties of the W-doped VO_2 nanoparticles were characterized by measuring the VO_2-PET composite film, which were prepared by casting VO_2 on a PET substrate with a fixed thickness. Fig. 12 and Table 2 show the variation in the transmittance spectra for different W doping contents. As the W doping content increased from 0 to 2.05%, the luminous transmittance (T_{lum}) decreased from 33.5 % to 14.4 % at 10 °C and 31.2% to 16.0% at 90 °C. In addition, the solar modulation ability (ΔT_{sol}) decreased from 16.0% to 8.8%. Therefore, the thermochromic optical property of VO_2 (M) deteriorated due to W doping. Moreover,

the ΔT_{sol} was approximately 16.0% when the W content ranged from 0 to 1.13% but rapidly decreased as the W content increased further. Due to the abnormal changes in T_{lum} (i.e. at 90 °C, T_{lum} was larger than that at 10 °C for a W content between 1.57 and 2.05%). Moreover, the infrared (IR) modulation at 1500 nm (ΔT_{1500}) steadily changed from 70.4% to 36.9%. Therefore, a good balance between the transition temperature (Tc) and optical properties (T_{lum}, ΔT_{sol} and ΔT_{1500}) is necessary. Since the required Tc was near the ambient temperature, the W doping content should be higher than 1.57% but the T_{lum} and ΔT_{sol} of the 1.57% W-doped VO_2 film were not sufficiently enough. Therefore, the optical properties should be further improved by various methods in our follow-up study (e.g. co-doping with other ions (Zr[32], Mg[33], F[34]), preparing nanoporous films[35], fabricating VO_2-based core/shell nanostructures(VO_2/SiO_2)[22, 36] and developing composite films (VO_2/TiO_2)[37].

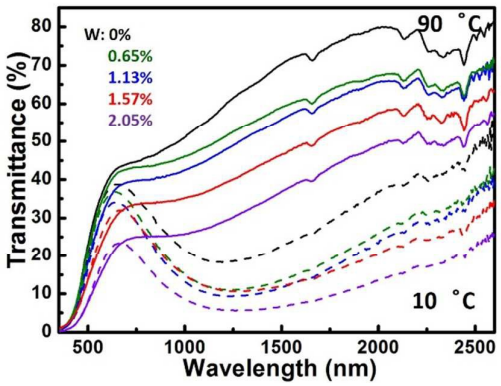

Fig. 12 Transmittance spectra at 25 °C and 90 °C for the W doped VO_2-PET composite films.

Table 2 Solar energy control properties of the VO_2-PET composite films with different VO_2 solid contents.

W doping content (%)	T_{lum}(%)		T_{sol}(%)		ΔT_{sol} (%)	ΔT_{1500} (%)
	20°C	90°C	20°C	90°C		
0	33.5	31.2	42.2	26.2	16.0	70.4
0.65	32.0	29.9	38.7	22.2	16.4	59.1
1.13	28.2	27.1	35.4	20.0	15.4	55.9
1.57	21.7	23.5	29.2	19.2	10.0	46.6
2.05	14.4	16.0	21.5	12.7	8.8	36.9

4 Conclusions

Combining the V_2O_5 and oxalic acid system with the homogeneous precipitation method, a novel system involving Routes A and B was proposed to study the influence of ammonium (NH_4^+) on the growth of VO_2 nanomaterial, by controlling the addition of the $NH_3 \cdot H_2O$ solution. In Route A without the addition of ammonium, VO_2 (B) nano-belts were assembled by a vanadium oxide hydrate $(VO_2)x \cdot yH_2O$. In Route B in the presence of ammonium, VO_2 (M) nanoparticles were decomposed by $(NH_4)_2V_4O_9$ sheets, which were piled up by $(VO_2)x \cdot yH_2O$. The two entirely different growth mechanisms were attributed to the addition of the ammonium solution. In Route B, the as-prepared VO_2 (M) nanoparticles had a high latent heat (ΔH = 32.4 J/g) during MIT, and a VO_2-PET composite film prepared by casting these VO_2 (M) nanoparticles exhibited excellent thermochromic optical properties (T_{lum} = 33.5%, ΔT_{sol} = 16.0%). Moreover, the W-doped VO_2 nanoparticles were prepared and the Tc reduction efficiency for different W doping contents ranging from 0 to 2.0% was determined to occur at a rate of 20 K/at.%.

Acknowledgements

This study was supported in part by funds from MOST (2014AA032802), NSFC (State Outstanding Young Scholars, 51325203) and Shanghai Municipal Science and Technology Commission (15XD1501700, 13NM1402200, 13521102100).

References

1. F. J. Morin, *Phys. Rev. Lett*, 1959, **34-36**, 34-36.
2. J. Booth and P. Casey, *Phys. Rev. Lett.*, 2009, **103**, 086402.
3. Y. F. Gao, H. J. Luo, Z. T. Zhang, L. T. Kang, Z. Chen, J. Du, M. Kanehira and C. X. Cao, *Nano Energy*, 2012, **1**, 221-246.
4. T. D. Manning, I. P. Parkin, M. E. Pemble, D. Sheel and D. Vernardou, *Chem. Mater.*, 2004, **16**, 744-749.
5. C. Z. Wu, J. Dai, X. D. Zhang, J. L. Yang, F. Qi, C. Gao and Y. Xie, *Angew. Chem. Int. Ed.*, 2010, **49**, 134-137.
6. S. D. Zhang, B. Shang, J. L. Yang, W. S. Yan, S. Q. Wei and Y. Xie, *Phys. Chem. Chem. Phys.*, 2011, **13**, 15873–15881.

7. J. Galy, *J. Solid State Chem.*, 1999, **148**, 224-228.
8. L. Liu, F. Cao, T. Yao, Y. Xu, M. Zhou, B. Y. Qu, B. C. Pan, C. Z. Wu, S. Q. Wei and Y. Xie, *New J. Chem.*, 2012, **36**, 619.
9. C. X. Cao, Y. F. Gao and H. J. Luo, *J. Phys. Chem. C*, 2008, **112**, 18810-18814.
10. C. Niu, J. Meng, C. Han, K. Zhao, M. Yan and L. Mai, *Nano Lett.*, 2014, **14**, 2873-2878.
11. Y. F. Gao, C. X. Cao, L. Dai, H. J. Luo, M. Kanehira, Y. Ding and Z. L. Wang, *Energy Environ. Sci*, 2012, **5**, 8708.
12. Z. Chen, Y. F. Gao, L. T. Kang, C. X. Cao, S. Chen and H. J. Luo, *J. Mater. Chem. A*, 2014, **2**, 2718.
13. L. Zhang, F. Xia, Z. Song, N. A. S. Webster, J. Song, H. Luo and Y. Gao, *Inorg. Chem. Front.*, 2016, **3**, 117-124.
14. S. Li, Y. Li, M. Jiang, S. Ji, H. Luo, Y. Gao and P. Jin, *ACS Appl. Mater. Interfaces*, 2013, **5**, 6453-6457.
15. L. Dai, Y. Gao, C. Cao, Z. Chen, H. Luo, M. Kanehira, J. Jin and Y. Liu, *RSC Adv.*, 2012, **2**, 5265.
16. W. Li, S. Ji, Y. Li, A. Huang, H. Luo and P. Jin, *RSC Adv.*, 2014, **4**, 13026.
17. S. Ji, Y. Zhao, F. Zhang and P. Jin, *J. Cryst. Growth*, 2010, **312**, 282-286.
18. C. X. Cao, Y. F. Gao, L. T. Kang and H. J. Luo, *CrystEngComm*, 2010, **12**, 4048-4051.
19. B. Dong, N. Shen, C. Cao, Z. Chen, H. Luo and Y. Gao, *Crystengcomm*, 2016, **18**, 558-565.
20. W. Shi, S. Song and H. Zhang, *Chem. Soc. Rev.*, 2013, **42**, 5714-5743.
21. N. Shen, B. Dong, C. Cao, Z. Chen, H. Luo and Y. Gao, *RSC Adv.*, 2015, **5**, 108015-108022.
22. Y. Zhou, S. Ji, Y. Li, Y. Gao, H. Luo and P. Jin, *J.Mater. Chem. C*, 2014, **2**, 3812.
23. J. Livage, *Coordin. Chem. Rev.*, 1998, **178**, 999-1018.
24. G. S. Zakharova, V. L. Volkov, C. Täschner, I. Hellmann, A. Leonhardt, R. Klingeler and B. Büchner, *Solid State Commun.*, 2009, **149**, 814-817.
25. G. S. Zakharova, C. Täschner, T. Kolb, C. Jahne, A. Leonhardt, B. Büchner and R. Klingeler, *Dalton Trans.*, 2013, **42**, 4897-4902.
26. P. Liu, K. Zhu, Y. Gao, Q. Wu, J. Liu, J. Qiu, Q. Gu and H. Zheng, *Crystengcomm*, 2013, **15**, 2753.
27. L. Whittaker, T. L. Wu, C. J. Patridge, G. Sambandamurthy and S. Banerjee, *J. Mater. Chem.*, 2011, **21**, 5580-5592.
28. A. Romanyuk, R. Steiner, L. Marot and P. Oelhafen, *Sol. Energ. Mat. Sol. C.*, 2007, **91**, 1831-1835.
29. X. G. Tan, T. Yao, R. Long, Z. H. Sun, Y. J. Feng, H. Cheng, X. Yuan, W. Q. Zhang, Q. H. Liu, C. Z. Wu, Y. Xie and S. Q. Wei, *Sci. Rep.*, 2012, **2**, 466.
30. T. C., G. P., F. M. E., C. J. B., N. M., K. G. S. and A. A., *Phys. Rev. B*, 1985, **31**, 1000-1011.
31. L. Whittaker, C. J. Patridge and S. Banerjee, *J. Phys. Chem. Lett.*, 2011, **2**, 745-758.
32. N. Shen, S. Chen, Z. Chen, X. Liu, C. Cao, B. Dong, H. Luo, J. Liu and Y. Gao, *J. Mater. Chem. A*, 2014, **2**, 15087.
33. J. Zhou, Y. Gao, X. Liu, Z. Chen, L. Dai, C. Cao, H. Luo, M. Kanahira, C. Sun and L. Yan, *Phys. Chem. Chem. Phys*., 2013, **15**, 7505-7511.
34. L. Dai, S. Chen, J. Liu, Y. Gao, J. Zhou, Z. Chen, C. Cao, H. Luo and M. Kanehira, *Phys. Chem. Chem. Phys*., 2013, 15, 11723-11729.
35. L. T. Kang, Y. F. Gao, H. J. Luo, Z. Chen, J. Du and Z. T. Zhang, *ACS Appl. Mater. Interfaces*,

2011, **3**, 135-138.

36. Y. F. Gao, S. B. Wang, H. J. Luo, L. Dai, C. X. Cao, Y. L. Liu, Z. Chen and M. Kanehira, *Energy Environ. Sci.*, 2012, **5**, 6104.

37. N. R. Mlyuka, G. A. Niklasson and C. G. Granqvist, *Sol. Energ. Mat. Sol. C.*, 2009, **93**, 1685-1687.